THE ASTROPHYSICAL JOURNAL, 547:1024–1033, 2001 February 1

PROBING THE INNER REGION OF CYGNUS X-1 IN THE LOW/HARD STATE THROUGH ITS X-RAY BROADBAND SPECTRUM

T. DI SALVO,[1] C. DONE,[2] P. T. ŻYCKI,[3] L. BURDERI,[4] AND N. R. ROBBA[1]
Received 2000 March 16; accepted 2000 October 2

ABSTRACT

We present the broadband X-ray spectrum of Cyg X-1 in the low/hard state as observed by the instruments on board *BeppoSAX*. The spectrum spans from 0.1 to 200 keV, allowing the total accretion luminosity to be observed rather than extrapolated, corresponding to $\sim 2\%$ of the Eddington limit for a 10 $M_\odot$ black hole. The broad bandpass allows us to determine the continuum shape with great accuracy. Simple models of Compton upscattering of seed photons from the accretion disk do not adequately match the spectrum. At low energies an additional continuum component is required, giving a complex soft excess which extends up to ~ 4 keV, in line with previous results from *ASCA*. Moreover, we clearly detect a reflected component from the accretion disk that is smeared, probably because of relativistic and Doppler effects. The reflecting material is not strongly ionized and does not subtend a large solid angle as seen from the corona ($\Omega/2\pi \sim 0.1$–0.3). The estimated inner radius of the disk, which depends on the inclination of the system, is most probably between 10 and 70 gravitational radii (R_g). An unsmeared reprocessed component, probably originating from the companion star or the outer disk, could also be present. In this case, the inner radius of the disk, as inferred from the smeared reflection, is smaller, between $6R_g$ and $20R_g$.

Subject headings: accretion, accretion disks — black hole physics — stars: individual (Cygnus X-1) — X-rays: general — X-rays: stars

1. INTRODUCTION

Cyg X-1 is the brightest of the persistent galactic black hole candidates (GBHCs). It is a binary system consisting of a black hole accreting matter from a supergiant type O star. It shows (at least) two different spectral states, namely, a high/soft state where the luminosity is dominated by strong blackbody emission at low energies ($kT = 0.5$–1 keV) and a steep power law (photon index $\Gamma > 2$–3), extending out to at least 800 keV, is also present, and a low/hard state, which has much less soft emission ($kT = 0.1$–0.3 keV) and has luminosity dominated by a hard power law ($\Gamma \sim 1.4$–1.9) that cuts off at ~ 200 keV. In addition to the continuum emission, other spectral features are present in the spectrum, most noticeably an iron Kα line and edge at 6.4 and 7.1 keV, respectively. These features are seen in both spectral states and can be fitted with models of X-ray reflection of the power law from an accretion disk (Done et al. 1992; Gierliński et al. 1997, 1999).

Detailed spectroscopy of the reflected spectrum can be used to probe the accretion flow since its amplitude and shape are determined by the ionization state, geometry, and velocity field of the reprocessing plasma. Ionization of the reprocessor decreases the photoabsorption opacity, thus increasing the reflection albedo at low energies as well as the energy and intensity of the iron Kα fluorescence/recombination line and energy and depth of the iron K edge (Lightman & White 1988; Ross & Fabian 1993; Życki et al. 1994). The normalization of the reflected spectrum for a given ionization then depends on the inclination angle of the accretion disk with respect to the observer and on the solid angle subtended by the disk to the hard X-ray source (George & Fabian 1991; Matt, Perola, & Piro 1991). The combination of Doppler effects from the high orbital velocities and strong gravity in the vicinity of a black hole smears the reflected spectrum, so the line (and the reflected continuum) has a characteristically skewed, broad profile whose detailed shape depends on the inclination and on how deeply the accretion disk extends into the black hole potential (Fabian et al. 1989).

The best known example of the effects mentioned above is the Fe Kα line profile in the spectrum of the Seyfert 1 galaxy MCG -6-30-15 (Tanaka et al. 1995). The amount of reflected spectrum is that expected for a disk which covers half the sky as seen from the X-ray source (Lee et al. 1999). The fit of the iron line profile implies that the inner edge of this reprocessor lies at (or even within) the marginally stable orbit in Schwarzschild metric $R_{\rm ms} = 6R_g$ ($R_g \equiv GM/c^2$, where G is the gravitational constant, M the mass of the black hole, and c the speed of light; Tanaka et al. 1995; Iwasawa et al. 1996). These effects should also be present in GBHCs and should be more easily observed because of the much higher signal-to-noise ratio. Yet in the low/hard state of Cyg X-1, the amount of observable reflection is smaller than expected for a complete disk (e.g., Gierliński et al. 1997), and the amount of relativistic smearing is less than that seen in MCG -6-30-15, implying that the disk terminates at $10R_g$–$20R_g$ rather than extending down to the last stable orbit (Done & Życki 1999). Other low/hard state data from GBHCs show the same lack of extreme relativistic smearing as Cyg X-1 (Życki, Done, & Smith 1997, 1998, 1999; Gilfanov, Churazov, & Revnivtsev 1999), as do some active galactic nuclei (IC 4329a, Done, Madejski, & Życki 2000; NGC 5548, Chiang et al. 2000). In this respect, MCG -6-30-15 has an exceptionally steep X-ray spectrum,

[1] Dipartimento di Scienze Fisiche ed Astronomiche, Università di Palermo, Via Archirafi 36, 90123 Palermo, Italy; disalvo@gifco.fisica.unipa.it.
[2] Department of Physics, University of Durham, South Road, Durham DH1 3LE, England, UK.
[3] Nicolaus Copernicus Astronomical Center, Bartycka 18, 00-716 Warsaw, Poland.
[4] Osservatorio Astronomico di Roma, Via Frascati 33, 00040 Monteporzio Catone, Roma, Italy.

so it is more comparable to the high/soft state of GBHCs rather than to the low/hard state discussed here (Zdziarski, Lubiński, & Smith 1999).

If the "standard" optically thick, geometrically thin disk does truncate before the last stable orbit, this could indicate that inside this transition radius ($R_{tr} > R_{ms}$) the accretion changes to a hot, optically thin, geometrically thick flow, most plausibly an advection-dominated accretion flow (ADAF; see, e.g., Narayan 1996 for a review). Such a geometrical configuration is compatible with the overall broadband spectral shape of Cyg X-1, which has a rather hard (photon-starved) spectrum, as well as with the observed low amplitude of reflection and relativistic smearing (Poutanen, Krolik, & Ryde 1997; Gierliński et al. 1997; Dove et al. 1997; review in Poutanen 1998). The alternative models which keep an untruncated disk are reviewed in Done & Życki (1999). These models require that the hard X-rays be produced in active regions above the disk, probably powered by magnetic reconnection (Galeev, Rosner, & Vaiana 1979; Haardt, Maraschi, & Ghisellini 1994). There are two plausible ways for the untruncated disk models to match the spectral constraints. First, there are the models in which the X-ray emission regions expand with relativistic velocities away from the disk (Beloborodov 1999a, 1999b). This suppresses both the seed photons for Compton scattering (so giving the observed hard spectrum) and the amount of reflection (by beaming the observed X-ray spectrum away from the disk). The second possibility is that the X-ray illumination photoionizes the disk, reducing the photoelectric opacity. In this case, there are no spectral features in the reflected spectrum since it is formed purely from Thomson scattering. The large fraction of flux reflected means that this also decreases the thermalized fraction of the primary X-rays, so there are few soft photons (Ross, Fabian, & Young 1999; Nayakshin, Kazanas, & Kallman 2000).

Distinguishing between these various models should surely be possible from detailed studies of the reflected spectrum and energetics of the continuum spectrum. However, the derived parameters for the amount of reflection and smearing depend crucially on how the continuum is modeled, and there is increasing evidence that simple thermal disk blackbody and Comptonized power laws are not sufficient to describe the spectrum, especially at low energies where *ASCA* data show an additional soft component below 3–4 keV in Cyg X-1 (Ebisawa et al. 1996). The continuum can be better characterized with a broad bandpass, and we report here on the *BeppoSAX* 0.1–200 keV observation of Cyg X-1 in the low/hard state. We show that there is indeed a complex soft component and that the reflected continuum can be clearly disentangled from this complex spectrum.

2. OBSERVATIONS

The *BeppoSAX* Narrow-Field Instruments (NFIs) observed Cyg X-1 on 1998 May 3 and 4 for an effective exposure time of 25 ks. The NFIs are four co-aligned instruments which cover more than three decades of energy, from 0.1 keV up to 200 keV, with good spectral resolution in the whole range. The Low-Energy Concentrator-Spectrometer (LECS; operating in the range 0.1–10 keV; Parmar et al. 1997) and Medium-Energy Concentrator-Spectrometer (MECS; 1–11 keV; Boella et al. 1997) have imaging capabilities with a field of view (FOV) of 20′ and 30′ radius, respectively. In these FOVs we selected the data for the scientific analysis in a circular region of 8′ and 4′ radius for LECS and MECS, respectively, around the centroid of the source. The background subtraction was obtained using blank sky observations in which we extracted the background data in a region of the FOV similar to that used for the source. The High-Pressure Gas Scintillation Proportional Counter (HPGSPC; 7–60 keV; Manzo et al. 1997) and Phoswich Detector System (PDS; 13–200 keV; Frontera et al. 1997) do not have imaging capabilities, because the FOVs, of $\sim 1^\circ$ FWHM, are delimited by collimators. The background subtraction for these instruments was obtained using the off-source data accumulated during the rocking of the collimators. The energy ranges used for each NFI are 0.12–3 keV for the LECS, 1.8–10 keV for the MECS, 8–30 keV for the HPGSPC, and 20–200 keV for the PDS. We added a (conservative) systematic error of 5% to the PDS data, to take into account calibration residuals.[5] Different normalizations of the four NFIs are considered by including in the model normalizing factors, fixed to 1 for the MECS and kept free for the other instruments. The same method has been used to fit Crab spectra (Massaro et al. 2000), obtaining photon indices which are within $\Delta\Gamma \sim 0.03$ of those expected from models of the synchrotron emission (Aharonian & Atoyan 1995).

During the *BeppoSAX* observation, Cyg X-1 was in its usual low/hard state with a total (0.1–200 keV) unabsorbed luminosity of $\sim 3 \times 10^{37}$ ergs s^{-1}, adopting a distance of 2 kpc (e.g., Massey, Johnson, & Degioia-Eastwood 1995; Malysheva 1997). Figure 1 shows the MECS light curves in three energy bands, 1–4 keV (*first panel, counting from top*), 4–7 keV (*second panel*) and 7–11 keV (*third panel*), and the corresponding hardness ratios (*fourth and fifth panels*). Although the MECS light curves show an increase of intensity up to $\sim 30\%$ during the observation, the hardness ratios appear to be constant, except for a little hardening at the end of the observing period (between 5.5×10^4 and 6×10^4 s). This hardening is probably due to an absorption dip, because it is visible in the soft range and disappears in the hard range. Cyg X-1 is known to show intensity dips, which preferentially occur near the superior conjunction, at the orbital phase $\phi = 0$, although dips were also observed at $\phi = 0.88$ and $\phi = 0.42$ (Ebisawa et al. 1996). The *BeppoSAX* observation spans the orbital phase interval $\phi = 0.39$–0.58 (using the ephemeris reported in Gies & Bolton 1982), and the observed dip occurs at phase $\phi = 0.51$. We excluded this dip from the following spectral analysis.

3. THE SPECTRAL MODEL

The direct Comptonized component from the corona is modeled by the *thComp* model (Zdziarski, Johnson, & Magdziarz 1996), obtained by solving the Kompaneets equation.

To describe the reflection component, we use the angle-dependent reflection model of Magdziarz & Zdziarski (1995) with a self-consistent iron emission line calculated for the given ionization state, temperature, spectral shape, and metal abundances, as described in detail in Życki et al. (1999). The total reprocessed component can be smeared to

[5] See the Web page at http://www.sdc.asi.it/software/cookbook/matrices.html.

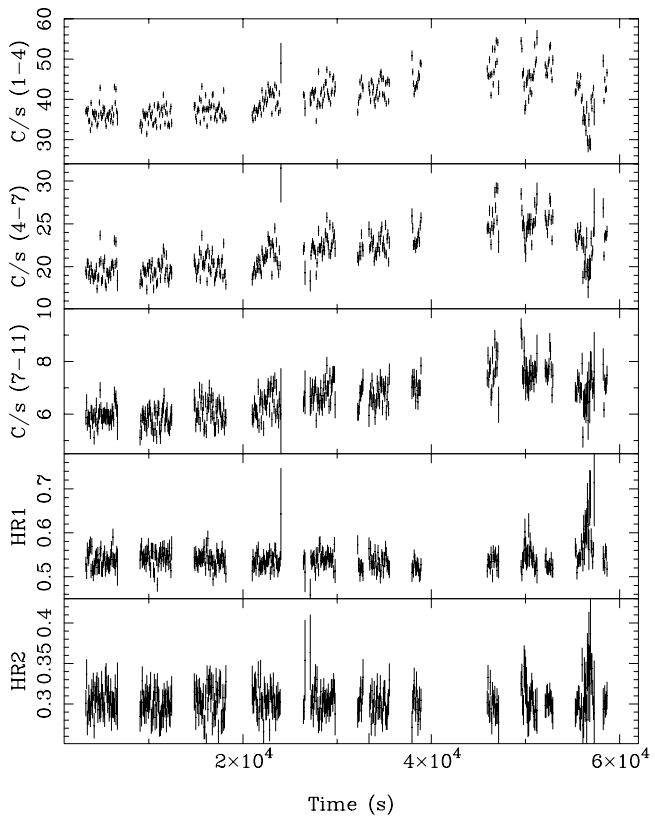

FIG. 1.—MECS light curves of Cyg X-1 in three energy bands: 1–4 keV (*first panel*, *counting from top*), 4–7 keV (*second panel*), and 7–11 keV (*third panel*); and the corresponding hardness ratios: HR1 = 4–7 keV/1–4 keV (*fourth panel*) and HR2 = 7–11 keV/4–7 keV (*fifth panel*).

take into account the relativistic and kinematic effects of disk emission (Fabian et al. 1989). This is done by convolving a spectrum with the XSPEC *diskline* model, parametrized by the inner and outer radius of the disk, $R_{\rm in}$ and $R_{\rm out}$, and the irradiation emissivity exponent, α, $F_{\rm irr} \propto r^{-\alpha}$. We fix $R_{\rm out} = 10^4 R_g$, $\alpha = 3$ and fit for $R_{\rm in}$, in order to obtain an estimate of the inner radius of the accretion disk.

The reflected spectrum also depends on the inclination of the system with respect to the line of sight. This parameter is more difficult to obtain for Cyg X-1 than for most other GBHCs since the companion O star loses matter via a strong wind, so it does not need to completely fill its Roche lobe in order to provide the accreting material. The lack of X-ray eclipses requires $i < 64°$, and almost all angles between this and $\sim 25°$ have been derived from spectrophotometric studies (see, e.g., Ninkov, Walker, & Yang 1987). Recent Doppler tomography studies of the Hα and He II lines set an upper limit to the inclination of 55° from the fact that the emission lines from the stream were not eclipsed (Sowers et al. 1998). However, this computation used the companion star radii of Gies & Bolton (1986), which have been shown to be overestimated (Herrero et al. 1995). Thus, we repeat the fits for a wider range of inclination angles to quantify how sensitive our results are to this parameter. Other unknown parameters affecting the reflected spectrum are the elemental abundances. We fix these at solar (Morrison & McCammon 1983), except for iron, which is allowed to vary.

4. SPECTRAL ANALYSIS

Spectral analysis was performed in XSPEC, Version 10 (Arnaud 1996), with all the nonstandard spectral models implemented as local models.

In Figure 2 we show the result of a fit of the 1.8–30 keV spectrum of Cyg X-1 with a simple photoelectric absorbed power law (the χ^2/degrees of freedom [dof] was 2008/274). In the residuals (in units of σ, *lower panel*), all the features expected in the Cyg X-1 spectrum are clearly visible, namely, the soft excess, the iron line and edge, and the spectral hardening due to the reflection at ~ 20 keV.

We tried to fit the 0.1–200 keV energy spectrum of Cyg X-1 with a simple model consisting of a direct Comptonized

TABLE 1

RESULTS OF THE FIT IN THE ENERGY BAND 0.1–200 keV

Parameter	Model 1	Model 2	Model 3	Model 4
$N_{\rm H}$ ($\times 10^{22}$ cm^{-2}).....	$0.70^{+0.12}_{-0.09}$	0.69 ± 0.11	0.74 ± 0.14	$0.85^{+0.13}_{-0.10}$
$kT_{\rm bb}$ (keV).....	$0.13^{+0.27}_{-0.01}$	0.130 ± 0.012	0.124 ± 0.014	0.112 ± 0.010
$F_{\rm bb}$.....	$0.049^{+0.075}_{-0.027}$	$0.045^{+0.062}_{-0.023}$	$0.07^{+0.13}_{-0.05}$	$0.16^{+0.26}_{-0.08}$
kT_{comptt} (keV)	$2.6^{+4.9}_{-0.7}$	$3.0^{+1.8}_{-0.9}$	3^{+10}_{-1}	2^{+10}_{-1}
τ_{comptt}	$8.6^{+2.4}_{-8.6}$	$8.3^{+2.4}_{-5.3}$	$7.5^{+2.2}_{-7.5}$	$5.7^{+6.8}_{-5.7}$
N_{comptt}	$0.79^{+0.76}_{-0.33}$	$0.65^{+0.59}_{-0.24}$	$0.8^{+1.3}_{-0.7}$	$4.0^{+3.6}_{-2.3}$
Photon index	1.614 ± 0.013	1.619 ± 0.015	1.627 ± 0.014	1.634 ± 0.013
kT_e (keV).....	111 ± 19	123^{+28}_{-20}	138^{+41}_{-24}	140^{+50}_{-35}
N_{thComp}	$1.086^{+0.047}_{-0.061}$	1.079 ± 0.050	$1.10^{+0.04}_{-0.13}$	1.205 ± 0.040
$f_{\rm rel}$.....	...	0.321 ± 0.033	$0.125^{+0.041}_{-0.060}$	0.185 ± 0.040
Fe abundance	1.0 (fixed)	1.0 (fixed)	1.0 (fixed)	2.0 (fixed)
cos i	0.6 (fixed)	0.6 (fixed)	0.6 (fixed)	0.78 (fixed)
ξ	$12.9^{+6.1}_{-5.1}$	$15.4^{+6.7}_{-4.6}$	90^{+500}_{-50}	35^{+25}_{-27}
$R_{\rm in}/R_g$	...	130^{+99}_{-45}	17^{+29}_{-7}	$6^{+5.5}$
$f_{\rm narrow}$	0.288 ± 0.027	...	$0.249^{+0.052}_{-0.066}$	0.12 ± 0.03
χ^2/dof.....	713/679	689/678	683/677	654/677

NOTES.—Error bars correspond to $\Delta\chi^2 = 2.7$. Blackbody flux is in units of L_{39}/D_{10}^2, where L_{39} is the luminosity in units of 10^{39} ergs s^{-1} and D_{10} is the distance in units of 10 kpc. *thComp* normalization is in photons cm^{-2} s^{-1} at 1 keV. $f = \Omega/2\pi$ is the reflection amplitude ($f = 1$ corresponds to the amplitude of reflection expected from a slab subtending a 2π solid angle around an isotropic source) and ξ is the ionization parameter, $\xi = L_{\rm X}/n_e r^2$.

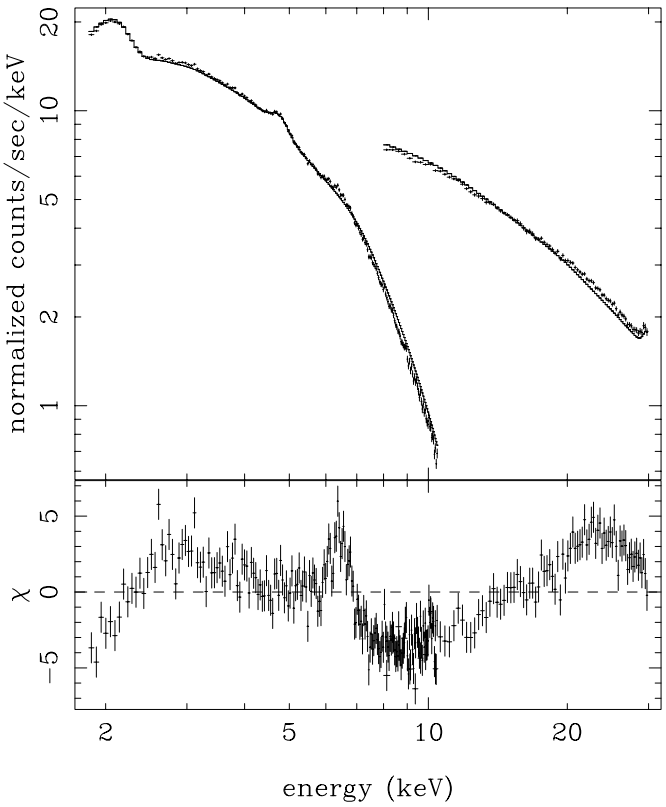

FIG. 2.—Result of a fit of the 1.8–30 keV spectrum of Cyg X-1 with a simple photoelectric absorbed power law (the χ^2/dof was 2008/274). *Upper panel*, MECS and HPGSPC data and model; *lower panel*, residuals (in unit of σ) with respect to the power law.

spectrum described by the *thComp* model, the corresponding reflected component, a blackbody to describe the soft emission, and photoelectric absorption by cold matter. The temperature of the soft seed photons for the Comptonization was fixed to the temperature of the blackbody. We also fixed the iron abundance to the solar value and $\cos i = 0.6$, where i is the inclination angle (see Done & Życki 1999). This model gives a poor fit, with χ^2/dof = 934/681. In the fit residuals, there are indications for a more complex shape of the soft component.

4.1. *The Soft Component*

Ebisawa et al. (1996), studying *ASCA* data of Cyg X-1 in the hard state, found that the shape of the soft component is not well described by a simple blackbody spectrum. They obtained a good fit using a blackbody plus a steep power-law tail. This is a rather unphysical description as the bolometric luminosity is infinite, so instead we use an additional Comptonized spectrum described by the *comptt* model (Titarchuk 1994). This improved the fit significantly, giving χ^2/dof = 713/679, using a reflection model without relativistic effects (model 1 in Table 1), and χ^2/dof = 689/678 considering the relativistic smearing of the reflection component (model 2 in Table 1). In both cases the seed photons for the additional Comptonized component were tied to the blackbody temperature, and the electron temperature was $\sim$3 keV. The optical depths reported in Table 1 are calculated for spherical geometry of the Comptonizing region; for a slab geometry, it is roughly half the previous value. The large uncertainties on the temperature and optical depth of this component are due to the fact that these parameters are correlated to each other and are not well constrained individually. We have also found that using a multicolor disk blackbody (*diskbb* in XSPEC; Mitsuda et al. 1984) instead of a blackbody to fit the soft emission does not improve the fit.

The soft excess is significantly detected using just the LECS and MECS data, showing that it is not an artifact of slight discrepancies in cross calibration between the instruments, amplified by the broad bandpass covered by *BeppoSAX*. A blackbody spectrum, together with a Comptonized continuum and relativistically smeared reflection, gives $\chi^2/dof = 566/437$, while adding the *comptt* component reduces this to χ^2/dof = 510/434.

Using an additional blackbody, with a temperature of $\sim$0.4 keV, instead of *comptt* as a description of the soft excess, we obtain χ^2/dof = 785/680, without relativistic smearing of the reflection component, and χ^2/dof = 749/679 considering the relativistic effects. The first description, using the *comptt* model for the soft excess, thus appears to be somewhat better, but we will consider both these possibilities in the discussion section.

Different descriptions of the soft excess give somewhat different estimates of the bolometric (unabsorbed) luminosity. In the first model (blackbody plus *comptt*), the unabsorbed flux in the two soft components is $F_{\rm soft} \approx 2.1 \times 10^{-8}$ ergs cm^{-2} s^{-1}, while it is only 3.3×10^{-9} ergs cm^{-2} s^{-1} in the second model (two blackbodies). Using a multicolor disk blackbody and *comptt*, we obtain rather larger $F_{\rm soft} \approx 7 \times 10^{-8}$ ergs cm^{-2} s^{-1}. The hard flux is the same in all models, $F_{\rm hard} \approx 3.8 \times 10^{-8}$ ergs cm^{-2} s^{-1}.

4.2. *The Hard Component*

Adopting now the blackbody plus *comptt* as a description of the soft component, we proceed to investigate the hard component in the spectrum.

4.2.1. *The Comptonized Continuum*

The Comptonized continuum is well described by the *thComp* model. The spectral slope derived from the data is $\Gamma \approx 1.67$, and the electron temperature is $kT_e \approx 140$ keV (these values were obtained for parameters of the reprocessed component $\cos i = 0.78$ and Fe abundance of 2 $\times$ solar [see § 4.2.2] but they are nearly independent of particular values chosen). The *thComp* model is known to give rather inaccurate temperature estimations for temperatures above $\sim$100 keV (A. Zdziarski 2000, private communication). We have therefore performed Monte Carlo simulations in order to derive the physical value of kT_e. Using the Monte Carlo code described in Appendix A of Życki et al. (1999), we obtain $kT_e \approx 90$ keV. The value of temperature is nearly independent of the plasma cloud geometry assumed, contrary to the value of optical depth, which we will discuss later in § 5.1.1.

4.2.2. *The Reprocessed Component*

The total model with the reprocessed component without relativistic smearing yields χ^2/dof = 713/679 (model 1 in Table 1). Allowing now for relativistic smearing of the reflection component, we obtain a better fit with χ^2/dof = 689/678 (model 2 in Table 1). An F-test demonstrates that the probability of chance improvement of the fit is

2×10^{-6}. In this case, the inner radius of the disk, as inferred from the reflection component, is $\sim 130 R_g$, and the reflection amplitude is $\Omega/2\pi \sim 0.3$, where Ω is the solid angle subtended by the reflector as viewed from the corona.

To constrain the iron abundance and the inclination angle i of the system, we fitted the data using different values of these two parameters. In particular, we considered $\cos i = 0.87$, 0.71, 0.60, 0.50 and [Fe] = 3, 2, 1.5, 1 × solar abundance (the grid of models for the Fe Kα line does not allow us to test Fe abundances greater than 3 × solar). The resulting values of χ^2 and $R_{\rm in}$ are reported in Table 2. We note that the inferred inner radius of the disk is strongly dependent on the inclination as well as iron abundance. Generally, we obtain larger radii in correspondence of high inclinations, because in this case the Doppler shifts, due to the orbital velocity of the matter, are stronger, giving substantial broadening. Nevertheless, we always obtain radii smaller than $150 R_g$, with the most probable values lower than $70 R_g$. The best overall fit is obtained for $\cos i = 0.87$ and [Fe] = 2, corresponding to an inner radius of $\sim 10 R_g$. However, we obtain an equivalently good fit for $\cos i = 0.78$ and [Fe] = 1.5, corresponding to an inner radius of $\sim 70 R_g$.

To compare the results, we plotted in Figure 3 the contributions to the χ^2 as a function of the energy in the iron line range for various models. Model 1 of Table 1 with a not relativistically smeared reflection is shown in the first panel (counting from top), the model corresponding to $\cos i = 0.78$ and [Fe] = 1.5 is shown in the second panel, and the model corresponding to $\cos i = 0.87$ and [Fe] = 2 is shown in the third panel. We note that while the model with $\cos i = 0.87$ and [Fe] = 2 can better fit the region around 5 keV, it leaves some residuals between 5.5 and 6.5 keV. On the other hand, the model with $\cos i = 0.78$ and [Fe] = 1.5 gives a better fit of the region between 5.5 and 6.5 keV. Because the latter seems to be better in the iron line region, this indicates that the inner radius of the disk is $\sim 70 R_g$ or that a more complex model is needed to fit the data.

A narrow (not relativistically smeared) and not ionized reflection component is also expected from the companion star and/or the outer flared disk, and it was actually observed in *ASCA* and Broad Band X-Ray Telescope data (Ebisawa et al. 1996; Done & Życki 1999). Adding to model 2 in Table 1 another reprocessed component, not ionized and not smeared, we obtain $\chi^2/{\rm dof} = 683/677$, i.e., a reduction of the χ^2 by $\Delta\chi^2 = 6$ (model 3 in Table 1). An *F*-test shows that this improvement is significant at the 99% confidence level for one additional parameter. Also in this case we fitted *BeppoSAX* data using different values of $\cos i$ and iron abundance. The resulting values of χ^2 and inner radius are reported in Table 3. In this case we obtain much smaller inner radii, around $10 R_g$–$20 R_g$, sometimes as small as $6 R_g$, i.e., the last stable orbit in the Schwarzschild metric. The best fit has $\cos i = 0.78$ and [Fe] = 2, corresponding to $R_{\rm in} \sim 6 R_g$. With these two parameters we obtain the results shown in Table 1 (model 4). In Figure 4*a* we show the Cyg

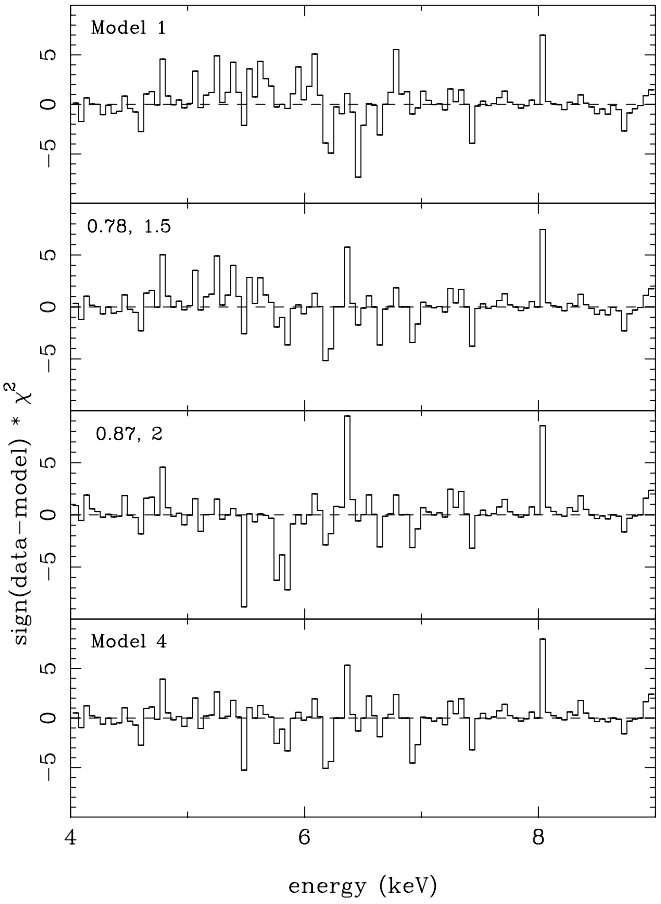

FIG. 3.—Contributions to the χ^2 as a function of the energy in the iron line range for various fit models. *First panel*: Model 1 of Table 1 with a not relativistically smeared reflection. *Second panel*: Model corresponding to $\cos i = 0.78$ and [Fe] = 1.5. *Third panel*: Model corresponding to $\cos i = 0.87$ and [Fe] = 2. *Fourth panel*: Model consisting of two reflection components for $\cos i = 0.78$ and [Fe] = 2 (model 4 in Table 1).

TABLE 2

RESULTS OF THE FIT IN THE 0.1–200 keV ENERGY RANGE WITH ONE REFLECTION COMPONENT

	INCLINATION (cos *i*)				
Fe ABUNDANCE	0.87	0.78	0.71	0.60	0.50
3	675 (8.3)	685 (6.0)	701 (42.5)	704 (34.7)	700 (47.7)
2	669 (9.85)	676 (40.2)	679 (52.4)	687 (57.3)	685 (76.6)
1.5	673 (15.6)	670 (69.0)	674 (79.7)	679 (84.5)	679 (109)
1	686 (49.4)	687 (91.4)	688 (117)	689 (130)	690 (167)

NOTES.—Results for different values of the inclination angle and of the iron abundance: χ^2 ($R_{\rm in}$), where $R_{\rm in}$ is in units of R_g and degrees of freedom is 678. Typical errors on $R_{\rm in}$ are as in Table 1.

TABLE 3

RESULTS OF THE FIT IN THE 0.1–200 keV ENERGY RANGE WITH TWO REFLECTION COMPONENTS

	INCLINATION (cos i)				
Fe ABUNDANCE	0.87	0.78	0.71	0.60	0.50
3	676 (6.0)	659 (6.0)	663 (6.0)	675 (12.0)	677 (15.0)
2	664 (9.5)	654 (6.0)	658 (10.2)	663 (14.3)	663 (17.5)
1.5	674 (6.0)	658 (6.0)	664 (6.0)	668 (16.8)	668 (20.9)
1	685 (6.0)	667 (6.0)	674 (6.0)	683 (17.3)	686 (26.4)

NOTES.—Results for different values of the inclination angle and of the iron abundance: χ^2 ($R_{\rm in}$), where $R_{\rm in}$ is in units of R_g and degrees of freedom is 677. Typical errors on $R_{\rm in}$ are as in Table 1. There is a clear trend in the χ^2 values to be smaller at supersolar iron abundance and for cos $i \sim 0.8$ ($i = 35°$–$40°$).

X-1 data fit using this model (*upper panel*) and the residuals (in unit of σ) with respect to the model (*lower panel*). The contributions to the χ^2 as a function of the energy in the iron line range are also shown in Figure 3 (*lower panel*).

The results are subtly different from those derived from the *ASCA* data (Done & Życki 1999), where the best fit was for somewhat higher inclination (cos $i = 0.75$–0.50 and [Fe] = 2), with correspondingly larger inner disk radii. We caution that at this level small uncertainties in the response and cross calibration become important.

A comparison of Tables 2 and 3 shows that the additional unsmeared component does not give a significant improvement of fit for all combinations of inclination and iron abundance considered, so we cannot say it is unambiguously detected in our data.

5. DISCUSSION

We analyzed the broadband (0.1–200 keV) spectrum of Cyg X-1 in the hard state observed by *BeppoSAX*. The total spectrum predicted by model 4 from Table 1 is plotted in

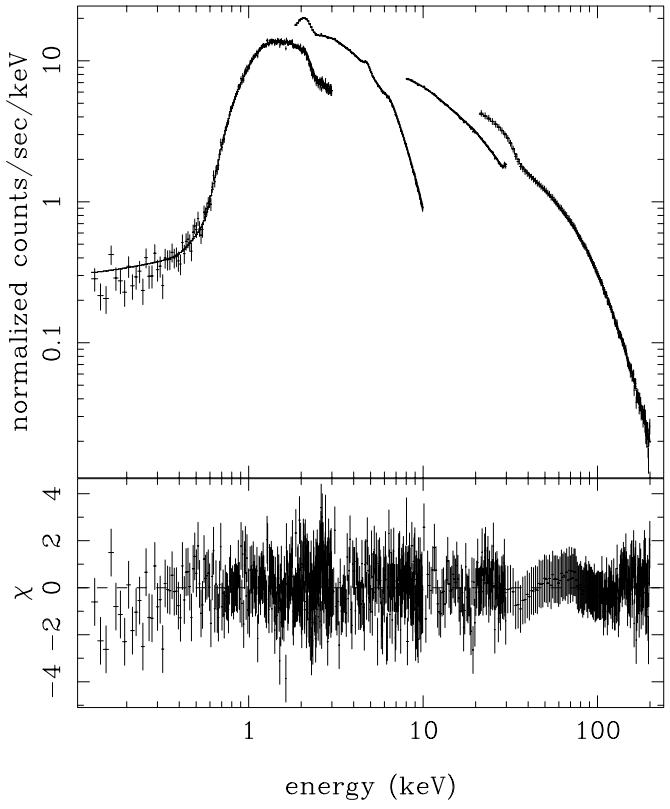

Fig. 4*a*

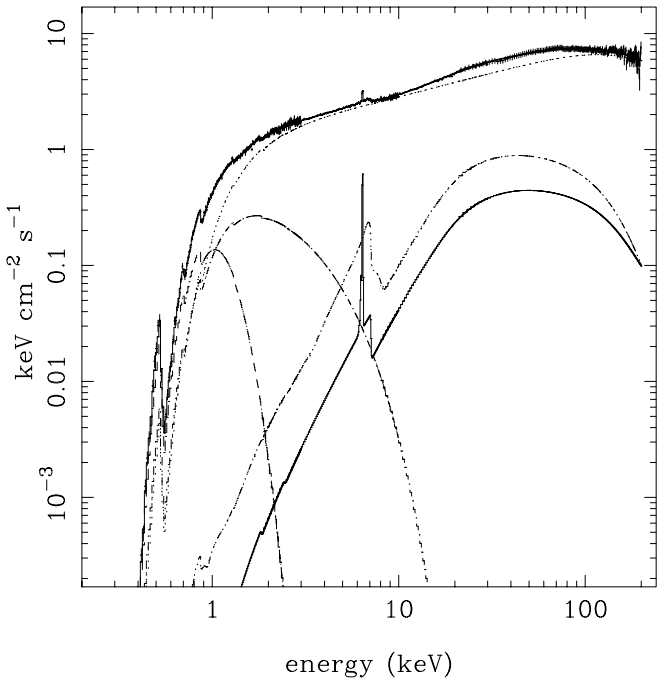

Fig. 4*b*

FIG. 4.—(*a*) Cyg X-1 data fit using model 4 of Table 1 (*upper panel*) and the residuals (in units of σ) with respect to the model (*lower panel*). (*b*) Cyg X-1 unfolded spectrum predicted by model 4 (Table 1; *shown as a solid line*). The single components of the model are also shown, namely, the soft component, described by the blackbody at ~0.1 keV (*dashed line*) and the low-temperature (~2 keV) Comptonized component (*dot-dashed line*), the hard Comptonized emission from a hot (~140 keV) corona (*dotted line*), and the corresponding narrow and smeared reprocessed components (*solid and dot-dot-dot-dashed lines*, respectively) containing the iron Kα line and edge and the reflected continuum.

Figure 4*b*. The overall spectrum consists of a complex soft component and a hard component. The former can be described by a blackbody (or disk blackbody) at $kT_0 \sim 0.1$ keV and an additional component that can be described by Comptonization of soft photons in a low-temperature ($kT \sim 2$ keV) plasma with moderate optical depth ($\tau \sim 6$ for a spherical geometry). This is plausible though not a unique description—the additional component can be, for instance, a second blackbody with $kT \approx 0.4$ keV.

Such a complex model for the soft excess in Cyg X-1 is in agreement with the results of Ebisawa et al. (1996), who fitted the soft component with a blackbody and a steep power-law tail. The presence of such additional Comptonized excesses is not uncommon in X-ray spectra of other accreting black holes. They were previously reported in the very high and high states of Nova Muscae 1991 (Życki et al. 1998), in the high state of GRS 1915+105 and GRO J1655−40 (Coppi 1999; Zhang et al. 2000), in the high state of Cyg X-1 (Gierliński et al. 1999), and also in the Seyfert 1 galaxy NGC 5548 (Magdziarz et al. 1998). They suggest existence of a third phase of accreting plasma, intermediate in properties between the cold, optically thick disk and the hot, optically thin matter responsible for the hard Comptonization. The origin and location of such warm plasma would be different in the three different scenarios discussed below.

The hard component can be modeled as Comptonized emission from a hot ($\sim$100 keV) corona, with the corresponding reprocessed component (Fe Kα line and edge and the reflected continuum). The reprocessed component has a small amplitude, $\Omega/2\pi \sim 0.1$–0.3, is smeared, and is not highly ionized. The best fit indicates high values of the iron abundance (2 × solar) and moderate inclination angles ($\cos i = 0.7$–0.8). A second not ionized and not smeared reflection can also be present, probably from the companion star and/or an outer flared disk.

Smearing of the reflected component is significantly detected in Cyg X-1. Assuming that it is due to relativistic effects, this indicates the presence of optically thick material at small radii. The value of the inner radius of the disk is strongly dependent on the inclination angle of the system and the iron abundance (and on details of the modeling and calibration). The model fits given in Table 3, using two reflected components, give values between $6R_g$ and $20R_g$. Without a second reflector, the inferred inner radius can be larger ($\sim 150R_g$ at most; see Table 2), but the fits are generally worse. These results are consistent with the inner radius of the disk inferred from the rapid timing variability properties, in the hypothesis that the quasi-periodic oscillation frequency detected in these systems is related to the innermost disk radius. In the case of Cyg X-1 in the low/hard state, $R_{\rm in}$ should be less than $\sim 20R_g$ (depending on the mass of the black hole; Di Matteo & Psaltis 1999).

Our broadband spectral results are in agreement with previous studies of the low/hard state of Cyg X-1 (Poutanen et al. 1997; Gierliński et al. 1997; Dove et al. 1997), where it was demonstrated that the observed spectra are incompatible with the model of an accretion disk with a static corona in a plane-parallel geometry (Haardt & Maraschi 1993). In these models, the soft photons emitted by the disk have to pass through the corona, resulting in a strong cooling. Therefore, the predicted spectra are too soft to match the observed hard spectrum from Cyg X-1. Instead, they can be interpreted within two geometrical scenarios: a hot inner disk with a cold outer disk and a disk with active regions. We will now discuss both geometries in some detail.

5.1. *The Hot Disk Model*

In the hot disk model, the hard X-ray spectrum originates in an inner accretion flow, with electron temperature $\sim$100 keV and optical depth $\tau_{\rm es} \sim 1$. If the hot flow is heated by a viscous (αP) mechanism (Shakura & Sunyaev 1973), the electron temperature has to be different from the ion temperature (Shapiro, Lightman, & Eardley 1976), in which case $T_{\rm ion}$ approaches the virial temperature, the flow becomes geometrically thick, and advective transfer of energy is important (Ichimaru 1977; Narayan & Yi 1995). Conduction of heat between the hot flow and any "standard" cold disk necessarily leads to evaporation of the disk if the accretion rate is smaller than a critical value (Różańska & Czerny 2000). This gives a mechanism for a transition between disk-dominated and hot-flow–dominated accretion, though there can be a region of overlap between the two flows (Różańska & Czerny 2000), where the observed additional soft component may be generated.

5.1.1. *Optical Depth of the Central Plasma Cloud*

We have performed Monte Carlo simulations of Comptonization in this geometry to estimate the optical depth of the central plasma cloud and the amplitude of the reprocessed component. Approximating the complex geometry to a central, uniform-density sphere and an outer cold disk, without any overlap, we find that the observed hard spectrum can be matched if $kT_e \approx 90$ keV and $\tau_{\rm es} \approx 1.8$. This then predicts the amplitude of the spectrum of the soft seed photons and the amount of reflected spectrum from the accretion disk. Both these predicted values are within the observed limits, if we use the *comptt* model to describe the soft excess. Using two blackbodies for the soft emission, the observed ratio $L_{\rm hard}/L_{\rm soft}$ is larger than the predicted value in the above geometry, without overlap between the outer disk and the central plasma cloud. We also note that the assumed uniform sphere may not be a good approximation to a real accretion flow, where energy dissipation is concentrated toward the center.

5.1.2. *The Overall Energetics*

Adopting the Comptonization model for the soft excess, we find the total flux in the hard component $F_{\rm hard} = 3.8 \times 10^{-8}$ ergs cm^{-2} s^{-1} and in the soft component (blackbody plus the soft Comptonized component) $F_{\rm soft} = 2.1 \times 10^{-8}$ ergs cm^{-2} s^{-1}. The bolometric luminosity of the primary source is then

$$L_{\rm tot} = L_{\rm hard} + L_{\rm soft} = 4\pi d^2 F_{\rm hard} + \frac{2\pi d^2}{\cos i} F_{\rm soft}\,, \qquad (1)$$

assuming isotropic emission of the hard X-ray source and disk emission of the soft X-ray source. This gives $L_{\rm tot} = 2.5 \times 10^{37} d_2^2$ ergs s^{-1} $\approx 0.02 d_2^2 M_{10}^{-1} L_{\rm Edd}$ for $\cos i = 0.7$, where d_2 is the distance to Cyg X-1 in units of 2 kpc, M_{10} is the black hole mass in units of 10 $M_\odot$, and $L_{\rm Edd}$ is the Eddington luminosity for a 10 $M_\odot$ black hole.

To compute the mass accretion rate, we need to take into account that a fraction of energy may be advected into the black hole. Denoting the advected fraction by $f_{\rm adv}$, we obtain the total rate of viscous energy dissipation, $Q^+ =$

$L_{\rm hard}/(1-f_{\rm adv})+L_{\rm soft}=L_{\rm tot}\{1+(L_{\rm hard}/L_{\rm tot})[f_{\rm adv}/(1-f_{\rm adv})]\}$. The mass accretion rate is then

$$\dot{M}=Q^{+}/(\eta c^{2})\approx 4.9\times 10^{17}d_{2}^{2}\left(1+\frac{L_{\rm hard}}{L_{\rm tot}}\frac{f_{\rm adv}}{1-f_{\rm adv}}\right)\ {\rm g\ s^{-1}}\ , \tag{2}$$

where $\eta=0.057$ is the efficiency of accretion in Schwarzschild metric. This gives

$$\dot{m}\equiv\frac{\dot{M}}{\dot{M}_{\rm Edd}}\approx 0.02d_{2}^{2}\,M_{10}^{-1}\left(1+\frac{L_{\rm hard}}{L_{\rm tot}}\frac{f_{\rm adv}}{1-f_{\rm adv}}\right), \tag{3}$$

for $\dot{M}_{\rm Edd}=L_{\rm Edd}/(\eta c^{2})\approx 2.5\times 10^{19}M_{10}$ g s^{-1}. For example, for $f_{\rm adv}=0.75$ (as in the solution of Zdziarski 1998 for $\dot{m}=\dot{m}_{\rm crit}$), $\dot{m}\approx 0.06d_{2}^{2}\,M_{10}$.

5.1.3. *Estimating the Transition Radius*

The transition radius does not enter the Monte Carlo simulations performed in § 5.1.1: the fraction of soft photons intercepted by the hard source is completely determined by the geometry, which is scale invariant. We can estimate the truncation radius using information from the total energy budget (§ 5.1.2). This again requires the assumption that there is relatively little overlap between the two phases and the cold disk emission is predominantly due to viscous energy dissipation rather than thermalization of the illuminating X-rays.

From equation (1) the fraction of viscous dissipation taking place in the hot flow is $Q_{\rm hot}^{+}/Q^{+}\approx 2/(3-f_{\rm adv})$. The radial distribution of energy dissipation per unit area of the disk is described by (e.g., Frank, King, & Raine 1992)

$$F(R)=\frac{3}{8\pi}\frac{GM\dot{M}}{R^{3}}\left(1-\sqrt{\frac{6R_{g}}{R}}\right). \tag{4}$$

Using equation (4) we can estimate $R_{\rm tr}$ solving

$$\frac{Q_{\rm hot}^{+}}{Q^{+}}=\frac{\int_{6R_{g}}^{R_{\rm tr}}2\pi F(R)R\,dR}{\int_{6R_{g}}^{\infty}2\pi F(R)R\,dR}\ . \tag{5}$$

For a purely radiative inner flow ($f_{\rm adv}=0$), we obtain $R_{\rm tr}\approx 40R_{g}$. The presence of advection increases this estimate, and for, e.g., $f_{\rm adv}=0.75$, we obtain $R_{\rm tr}\approx 130R_{g}$.

Alternatively, the inner radius of the cold disk can be estimated using the information on the blackbody soft component, assuming that this represents the emission from the inner part of a standard, optically thick, geometrically thin accretion disk. Its luminosity is then the total potential energy that has been released at $R_{\rm in}$:

$$L_{\rm bb}\simeq\frac{GM\dot{M}}{2R_{\rm in}}\ . \tag{6}$$

We attribute the measured temperature of the blackbody to the maximum temperature in the disk, which is reached at the inner radius $R_{\rm in}$ where the disk is truncated:

$$T_{\rm max}=\left(\frac{3GM\dot{M}}{8\pi\sigma R_{\rm in}^{3}}\right)^{1/4}\left(1-\sqrt{\frac{6R_{g}}{R_{\rm in}}}\right)^{1/4}\ . \tag{7}$$

From these two equations, we can find the inner radius of the disk as a function of the measured temperature and luminosity of the blackbody. Using the values reported in Table 1 (model 4) and considering that $L_{\rm disk}=2\pi d^{2}F_{\rm Earth}/\cos i$, where $F_{\rm Earth}$ is the observed flux, we obtain $R_{\rm in}(\cos i)^{1/2}\simeq 35R_{g}$, for a distance of 2 kpc.

This should be modified since a simple blackbody spectrum does not adequately describe the emission of accretion disks in X-ray binaries, because electron scattering modifies the spectrum (Shakura & Sunyaev 1973; White, Stella, & Parmar 1988). In this case, the measured color temperature is related to the effective temperature of the inner disk $T_{\rm col}=f_{\rm col}T_{\rm eff}$, where $f_{\rm col}$ is the spectral hardening factor. The factor $f_{\rm col}$ has been estimated by Shimura & Takahara (1995) to be ~ 1.7 for a luminosity of $\sim 10\%$ of the Eddington limit, with a little dependence on the mass of the compact object and the radial position. Applying this correction to the values of $R_{\rm in}$ obtained above, we find $R_{\rm eff}(\cos i)^{1/2}=f_{\rm col}^{2}R_{\rm in}(\cos i)^{1/2}\sim 100R_{g}$. The correction factor used here is probably an underestimate since Shimura & Takahara (1995) do not consider illuminated disks, as in the case of Cyg X-1. For instance, the additional soft excess component could be the emission of the inner part of the disk, strongly modified by Comptonization, which would then imply $f_{\rm col}\sim 4$–5. However, we are only considering here the part of the disk (probably at large radii) that emits the blackbody spectrum. Therefore, this region is probably not dramatically influenced by Comptonization, and a factor 1.7 could be good enough for this rough estimate.

5.1.4. *Summary of Hot Disk Model*

The geometry with a central, uniform-density, hot-plasma cloud with no overlap between this and an outer disk can reproduce the overall observed emission. Energy balance and the observed soft seed photon temperature both point to a transition radius between the disk and the hot flow of $\sim 100R_{g}$, in agreement with the estimation of the inner disk radius from the observed smearing of the iron line (assuming that this arises from relativistic effects), when only one reflection component is considered (see Table 2). However, this is in conflict with the smearing of the iron line in the best-fit models with two reflection components. For this model to fit the observations requires that there is further smearing of the reflected component by Comptonization (see § 5.2.2) and/or consideration of a more realistic geometry, with a hot flow that is centrally concentrated and where there is some overlap between the hot and cold flows.

5.2. *The Active Regions Model*

Another possibility for explaining hard spectra such as those observed from Cyg X-1 and other GBHCs is a geometry of an untruncated, cold disk with clumpy active regions (Stern et al. 1995). These can be physically envisioned as magnetic flares (Galeev et al. 1979; Haardt et al. 1994). However, in order to decrease the amplitude of the reprocessed component in such a configuration, one has to postulate that either the Comptonizing plasma is not static but outflows at mildly relativistic speed, $\beta\sim 0.3$ (Beloborodov 1999a, 1999b) or a hot ionized skin forms on top of the disk, increasing the X-ray albedo, reducing both the amplitude of the observed reflection and the soft, thermalized flux (Ross et al. 1999; Nayakshin et al. 2000).

5.2.1. *The Outflow Model*

Using the formulae from Beloborodov (1999a, 1999b), we can estimate the outflow velocity, β (in units of the speed of light), the flare geometry (parameterized by μ_{s}, the cosine of the angle between the midpoint of the flare and its edge as seen from the disk), and the fraction of energy dissipated in

the magnetic corona, $f_{\rm cor}$, from the observed spectral index $\Gamma \approx 1.63$, reflection amplitude $f \approx 0.2$–0.3, and ratio of luminosities, $L_{\rm soft}/L_{\rm hard} \sim 0.5$.

Equation (4) of Beloborodov (1999a) for the soft luminosity intercepted by the blob can be generalized to the case of $f_{\rm cor} < 1$ to give

$$L_{s,\,\rm blob} = \int_{-1}^{-\mu_s} [(1-a)L_{\rm X}(\mu) + (1-f_{\rm cor})L_{\rm tot}]\,d\mu\,, \quad (8)$$

where $a \sim 0.3$ is the energy-integrated X-ray albedo. $L_{\rm tot}$ is the total energy dissipation rate, $L_{\rm X} = f_{\rm cor}L_{\rm tot}$ is the blob (hard X-ray) luminosity, and we have assumed the same distribution of emission for both soft X-ray components (the blackbody/disk-blackbody and additional soft X-ray emission). This would be roughly equivalent to assuming the covering fraction of the active regions not much less than 1, so that the spatial distribution of the disk effective temperature is roughly uniform. The angular distribution of $L_{\rm X}$ in the observer frame is given by

$$L_{\rm X}(\mu) = \frac{L_{\rm X}}{2\gamma^4(1-\beta\mu)^3}\,. \quad (9)$$

Beloborodov (1999a) demonstrated that the soft luminosity in the comoving frame is $L_s^c = L_{s,\,\rm blob}\gamma^2[1-\beta(1+\mu_s)/2]$. The amplification factor $A \equiv L_{\rm X}/L_s^c$ can then be directly related to the hard X-ray slope $\Gamma \approx 2.33(A-1)^{-\delta}$, where $\delta \approx 1/6$ for GBHCs (Beloborodov 1999a, 1999b). Next, the observed soft X-ray luminosity, i.e., *not* intercepted by the blob, is

$$L_{\rm soft} = \int_{-\mu_s}^{0} [(1-a)L_{\rm X}(\mu) + (1-f_{\rm cor})L_{\rm tot}]\,d\mu\,, \quad (10)$$

while the observed hard X-ray luminosity is $L_{\rm hard} = L_{\rm X}(\cos i)$, where i is the inclination of the system. The three observables, Γ, f, and $L_{\rm soft}/L_{\rm hard}$, enable estimation of β, μ_s, and $f_{\rm cor}$ (assuming the inclination is known).

First, the outflow velocity can be directly obtained from the observed amplitude of reflection. For $f = 0.2$–0.3 and $\cos i = 0.75$, we obtain $\beta = 0.3$–0.4. Assuming for concreteness $\beta = 0.35$, we find that $f_{\rm cor} \approx 0.8$ and $\mu_s \approx 0.5$ reproduce both $\Gamma \approx 1.6$ and $L_{\rm soft}/L_{\rm hard} \approx 0.5$ in the spectral model containing the Comptonized excess. For the other model of the soft component (two blackbodies), which gives much smaller $L_{\rm soft}/L_{\rm hard} \approx 0.1$, the coronal dissipation fraction is $f_{\rm cor} > 0.99$, while $\mu_s \approx 0.3$.

A further development of the original model by Beloborodov (1999a) may also be necessary in light of the results on relativistic smearing of the reprocessed component. The outflow velocity has to be larger in the inner disk region than in the outer one, if the reprocessed component does not show the extreme smearing, corresponding to inner disk radius close to the last stable orbit at $6R_g$. However, our results here are somewhat ambiguous, and, in particular, in the model with two reprocessed components, the relativistic smearing does indeed correspond to inner radius close to $R_{\rm ms}$. The approximation with constant $\beta(r)$ may thus be appropriate.

5.2.2. *The Hot Skin Model*

In this model, assuming the disk is radially uniform, the observed amplitude of cold reflection can be expressed as

$$f \sim \frac{[P_{\rm trans}(\tau)]^2}{1+P_{\rm refl}(\tau)}\,, \quad (11)$$

where τ is the optical depth of the hot skin, while $P_{\rm trans}(\tau)$ and $P_{\rm refl}(\tau)$ are transmission and reflection probabilities *in the hot skin* (i.e., the ratio to the incident flux of the flux transmitted down through the hot skin to the cold material and the flux reflected out of the top of the hot skin, respectively). Obviously, for a pure scattering layer, $P_{\rm trans}(\tau) + P_{\rm refl}(\tau) = 1$. We obtained both probabilities from Monte Carlo simulations in a slab geometry. The observed amplitude, $f_{\rm rel} \approx 0.3$, corresponds to $P_{\rm trans}(\tau) \approx 0.64$ and $\tau \approx 0.7$.

The ratio of the soft thermalized flux to the primary hard X-ray flux is $(1-a)P_{\rm trans}(\tau)/[1+P_{\rm refl}(\tau)] \approx 0.4$, close to that observed in the model with the additional soft excess component described as Comptonized emission (see § 5.1.2). Indeed, one could imagine that this additional component is the disk emission Comptonized in the hot skin, as the photons diffuse through it. The expected ratio of fluxes of the blackbody component, $F_{\rm bb}$, to the Comptonized soft excess component, $F_{\rm sxe}$, is $F_{\rm bb}/F_{\rm sxe} \approx P_{\rm trans}/[A(1-P_{\rm trans})]$, where A is the Compton amplification. For an optical depth of 0.7, $F_{\rm bb}/F_{\rm sxe}$ should thus be ≈ 2 ($A - 1 \ll 1$ here), while from the best-fit model we infer $F_{\rm bb}/F_{\rm sxe} \approx 4$. Also, for an optical depth of ~ 0.7, the spectral shape of the additional Comptonized component requires that the temperature of the hot skin is $kT_{\rm skin} \approx 12$ keV. This is a little high compared to the mean Compton temperature in the skin of $kT_{\rm IC} \approx 5$ keV (Nayakshin et al. 2000).

The diffusion of the reprocessed photons through the hot skin results in smearing of iron spectral features due to Comptonization. We have modeled this by convolving the reprocessed spectrum with the Comptonization Green's functions of Titarchuk (1994). The smearing in the data is consistent with Comptonization alone for $kT_{\rm skin} = 12$ keV and $\tau = 0.7$: fitting only MECS data in the 4–10 keV band, we have found that Comptonization smearing gives $\chi^2/{\rm dof} = 130/126$, while relativistic smearing gives $\chi^2/{\rm dof} = 127/125$. However, in the hot skin model, there is no reason for the disk to be truncated, and so both smearing mechanisms would operate. The relativistic smearing would be that expected from a disk extending to $6R_g$, although with emissivity going to zero at the last stable orbit (Shakura & Sunyaev 1973), $F_{\rm irr}(r) \propto r^{-3}[1-(6R_g/r)^{1/2}]$. We have found that the model with both the relativistic smearing (with the inner radius fixed at $6R_g$) and Comptonization smearing (with fixed $\tau = 0.7$ and $kT = 11$ keV) gives a rather bad fit, $\chi^2/{\rm dof} = 150/126$. The problem may be avoided by postulating that the hot skin is thicker closer to the black hole (Nayakshin 2000), thus reducing the reflection amplitude from the inner regions.

5.2.3. *Summary of Untruncated Disk Models*

A fundamental problem is the high coronal dissipation required for these magnetic flare models. The maximum that has so far been produced in current (though admittedly incomplete) simulations is $f_{\rm cor} \sim 0.25$ (Miller & Stone 2000), while the data imply $f_{\rm cor} > 0.5$. Apart from this, the plasma outflow model can reproduce the observations, though the complex soft excess is unexplained. The hot skin model gives qualitative origin for the soft excess as Compton scattering of the disk photons, but quantitatively this does not give what is observed. Also, the Comptonization in the hot skin gives an additional smearing of the iron line and the reprocessed spectrum, and this smearing is much larger than that observed. However, if the model is extended to allow radial stratification of the depth of the hot skin, then

this may allow both the soft excess and line smearing to match those observed.

6. CONCLUSIONS

Broadband 0.1–200 keV *BeppoSAX* data from Cyg X-1 in low/hard state can be described by a complex soft component and a Comptonized hard component with the corresponding X-ray reprocessed spectrum. The soft component can be decomposed into a low-temperature ($kT \approx 0.1$ keV) blackbody emission, presumably from the accretion disk, and an additional component which can be modeled as Comptonization of the disk emission by a low-temperature ($kT \sim 2$ keV) plasma. The hard Comptonized component corresponds to a spectrum with photon index ~ 1.6 with a cutoff at the electron temperature of the corona, $kT_e \sim 100$ keV. The reflection spectrum consists of a weakly ionized, smeared component. Assuming that this broadening is due to relativistic smearing, this corresponds to an inner disk radius of $\sim 70R_g$ or $\sim 10R_g$ (depending on the inclination of the system). A nonsmeared component, due to reflection from the companion star and/or a flared outer disk, might also be present. In this case, we find that the inner radius of the disk, as deduced by the reflection component, is smaller, $\sim 6R_g$–$10R_g$.

The spectrum is broadly compatible with the three major scenarios proposed for emission in GBHCs, although all need some modification to fit the data. These are (1) a hot ($kT_e \sim 100$ keV), optically thin(ish), inner flow and a cold outer accretion disk; and an accretion disk with active regions with either (2) mildly relativistic outflow ($v \sim 0.3c$) of the Comptonizing plasma or (3) a hot ($kT \sim 10$ keV), ionized skin.

We thank B. Czerny and A. Zdziarski for useful discussions. This work was supported by the Italian Space Agency (ASI), by the Ministero della Ricerca Scientifica e Tecnologica (MURST), and in part by Polish KBN grants 2P03D01816 and 2P03D01718.

REFERENCES

Aharonian, F. A., & Atoyan, A. M. 1995, Astropart. Phys., 3, 275
Arnaud, K. A. 1996, in ASP Conf. Ser. 101, Astronomical Data Analysis Software and Systems V, ed. G. H. Jacoby & J. Barnes (San Francisco: ASP), 17
Beloborodov, A. M. 1999a, ApJ, 510, L123
———. 1999b, in ASP Conf. Ser. 161, High Energy Processes in Accreting Black Holes, ed. J. Poutanen & R. Svensson (San Francisco: ASP), 295
Boella, G., et al. 1997, A&AS, 122, 327
Chiang, J., Reynolds, C. S., Blaes, O. M., Nowak, M. A., Murray, N., Madejski, G., Marshall, H. L., & Magdziarz, P. 2000, ApJ, 528, 292
Coppi, P. S. 1999, in ASP Conf. Ser. 161, High Energy Processes in Accreting Black Holes, ed. J. Poutanen & R. Svensson (San Francisco: ASP), 375
Di Matteo, T., & Psaltis, D. 1999, ApJ, 526, L101
Done, C., Madejski, G. M., & Życki, P. T. 2000, ApJ, 536, 213
Done, C., Mulchaey, J. S., Mushotzky, R. F., & Arnaud, K. A. 1992, ApJ, 395, 275
Done, C., & Życki, P. T. 1999, MNRAS, 305, 457
Dove, J. B., Wilms, J., Maisack, M., & Begelman, M. C. 1997, ApJ, 487, 759
Ebisawa, K., et al. 1996, ApJ, 467, 419
Fabian, A. C., Rees, M. J., Stella, L., & White, N. E. 1989, MNRAS, 238, 729
Frank, J., King, A., & Raine, D. 1992, Accretion Power in Astrophysics (Cambridge Astrophysics Ser. 21; Cambridge: Cambridge Univ. Press)
Frontera, F., et al. 1997, A&AS, 122, 357
Galeev, A. A., Rosner, R., & Vaiana, G. S. 1979, ApJ, 229, 318
George, I. M., & Fabian, A. C. 1991, MNRAS, 249, 352
Gierliński, M., Zdziarski, A. A., Done, C., Johnson, W. N., Ebisawa, K., Ueda, Y., Haardt, F., & Phlips, B. F. 1997, MNRAS, 288, 958
Gierliński, M., Zdziarski, A. A., Poutanen, J., Coppi, P. S., Ebisawa, K., & Johnson, W. N. 1999, MNRAS, 309, 496
Gies, D. R., & Bolton, C. T. 1982, ApJ, 260, 240
———. 1986, ApJ, 304, 371
Gilfanov, M., Churazov, E., & Revnivtsev, M. 1999, A&A, 352, 182
Haardt, F., & Maraschi, L. 1993, ApJ, 413, 507
Haardt, F., Maraschi, L., & Ghisellini, G. 1994, ApJ, 432, L95
Herrero, A., Kudritzki, R. P., Gabler, R., Vilchez, J. M., & Gabler, A. 1995, A&A, 297, 556
Ichimaru, S. 1977, ApJ, 214, 840
Iwasawa, K., et al. 1996, MNRAS, 282, 1038
Lee, J. C., Fabian, A. C., Brandt, W. N., Reynolds, C. S., & Iwasawa, K. 1999, MNRAS, 310, 973
Lightman, A. P., & White, T. R. 1988, ApJ, 335, 57
Magdziarz, P., Blaes, O. M., Zdziarski, A. A., Johnson, W. N., & Smith, D. A. 1998, MNRAS, 301, 179
Magdziarz, P., & Zdziarski, A. A. 1995, MNRAS, 273, 837
Malysheva, L. K. 1997, Astron. Lett., 23, 585
Manzo, G., Giarrusso, S., Santangelo, A., Ciralli, F., Fazio, G., Piraino, S., & Segreto, A. 1997, A&AS, 122, 341
Massaro, E., Cusumano, G., Litterio, M., & Mineo, T. 2000, A&A, 361, 695
Massey, P., Johnson, K. E., & Degioia-Eastwood, K. 1995, ApJ, 454, 151
Matt, G., Perola, G. C., & Piro, L. 1991, A&A, 247, 25
Miller, K. A., & Stone, J. M. 2000, ApJ, 534, 398
Mitsuda, K., et al. 1984, PASJ, 36, 741
Morrison, R., & McCammon, D. 1983, ApJ, 270, 119
Narayan, R. 1996, in IAU Colloq. 163, Accretion Phenomena and Related Outflows, ed. D. T. Wickramasinghe, G. Bicknell, & L. Ferrario (ASP Conf. Ser. 121; San Francisco: ASP), 75
Narayan, R., & Yi, I. 1995, ApJ, 452, 710
Nayakshin, S. 2000, ApJ, 534, 718
Nayakshin, S., Kazanas, D., & Kallman, T. R. 2000, ApJ, 537, 833
Ninkov, Z., Walker, G. A. H., & Yang, S. 1987, ApJ, 321, 425
Parmar, A. N., et al. 1997, A&AS, 122, 309
Poutanen, J. 1998, in Theory of Black Hole Accretion Disks, ed. M. A. Abramowicz, G. Bjornsson, & J. E. Pringle (Cambridge: Cambridge Univ. Press), 100
Poutanen, J., Krolik, J. H., & Ryde, F. 1997, MNRAS, 292, L21
Ross, R. R., & Fabian, A. C. 1993, MNRAS, 261, 74
Ross, R. R., Fabian, A. C., & Young, A. J. 1999, MNRAS, 306, 461
Różańska, A., & Czerny, B. 2000, A&A, 360, 1170
Shakura, N. I., & Sunyaev, R. A. 1973, A&A, 24, 337
Shapiro, S. L., Lightman, A. P., & Eardley, D. M. 1976, ApJ, 204, 187
Shimura, T., & Takahara, F. 1995, ApJ, 445, 780
Sowers, J. W., Gies, D. R., Bagnuolo, W. G., Shafter, A. W., Wiemker, R., & Wiggs, M. S. 1998, ApJ, 506, 424
Stern, B. E., Poutanen, J., Svensson, R., Sikora, M., & Begelman, M. C. 1995, ApJ, 449, L13
Tanaka, Y., et al. 1995, Nature, 375, 659
Titarchuk, L. 1994, ApJ, 434, 570
White, N. E., Stella, L., & Parmar, A. N. 1988, ApJ, 324, 363
Zdziarski, A. A. 1998, MNRAS, 296, L51
Zdziarski, A. A., Johnson, W. N., & Magdziarz, P. 1996, MNRAS, 283, 193
Zdziarski, A. A., Lubiński, P., & Smith, D. A. 1999, MNRAS, 303, L11
Zhang, S. N., Cui, W., Chen, W., Yao, Y., Zhang, X., Sun, X., Wu, X., & Xu, H. 2000, Science, 287, 1239
Życki, P. T., Done, C., & Smith, D. A. 1997, ApJ, 488, L113
———. 1998, ApJ, 496, L25
———. 1999, MNRAS, 305, 231
Życki, P. T., Krolik, J. H., Zdziarski, A. A., & Kallman, T. R. 1994, ApJ, 437, 597